The high-pressure anisotropic thermoelastic properties of a potential inner core carbon-bearing phase, Fe₇C₃, by single-crystal X-ray diffraction

Xiaojing Lai[1,2,*,†], **Feng Zhu**[2,3], **Jiachao Liu**[4], **Dongzhou Zhang**[2], **Yi Hu**[1,2],
Gregory J. Finkelstein[2], **Przemyslaw Dera**[2], and **Bin Chen**[2,*]

[1]Department of Geology and Geophysics, University of Hawaiʻi at Mānoa, Honolulu, Hawaii 96822, U.S.A.
[2]Hawaii Institute of Geophysics and Planetology, University of Hawaiʻi at Mānoa, Honolulu, Hawaii 96822, U.S.A.
[3]Department of Earth and Environmental Sciences, University of Michigan, Ann Arbor, Michigan 48109, U.S.A.
[4]Department of Geological Sciences, Jackson School of Geosciences, University of Texas at Austin, Austin, Texas 78712, U.S.A.

Abstract

Carbon has been suggested as one of the light elements existing in the Earth's core. Under core conditions, iron carbide Fe₇C₃ is likely the first phase to solidify from a Fe-C melt and has thus been considered a potential component of the inner core. The crystal structure of Fe₇C₃, however, is still under debate, and its thermoelastic properties are not well constrained at high pressures. In this study, we performed synchrotron-based single-crystal X-ray diffraction experiment using an externally heated diamond-anvil cell to determine the crystal structure and thermoelastic properties of Fe₇C₃ up to 80 GPa and 800 K. Our diffraction data indicate that Fe₇C₃ adopts an orthorhombic structure under experimentally investigated conditions. The pressure-volume-temperature data for Fe₇C₃ were fitted by the high-temperature Birch-Murnaghan equation of state, yielding ambient-pressure unit-cell volume $V_0 = 745.2(2)$ Å³, bulk modulus $K_0 = 167(4)$ GPa, its first pressure derivative $K_0' = 5.0(2)$, $\mathrm{d}K/\mathrm{d}T = -0.02(1)$ GPa/K, and thermal expansion relation $\alpha_T = 4.7(9) \times 10^{-5} + 3(5) \times 10^{-8} \times (T - 300)$ K⁻¹. We also observed anisotropic elastic responses to changes in pressure and temperature along the different crystallographic directions. Fe₇C₃ has strong anisotropic compressibilities with the linear moduli $M_a > M_c > M_b$ from zero pressure to core pressures at 300 K, rendering the b axis the most compressible upon compression. The thermal expansion of c^3 is approximately four times larger than that of a^3 and b^3 at 600 and 700 K, implying that the high temperature may significantly influence the elastic anisotropy of Fe₇C₃. Therefore, the effect of high temperature needs to be considered when using Fe₇C₃ to explain the anisotropy of the Earth's inner core.

Keywords: Iron carbide, thermal equation of state, anisotropy, inner core, temperature effect; Physics and Chemistry of Earth's Deep Mantle and Core

Introduction

Earth's inner core is considered to consist primarily of iron alloyed with nickel and one or more light elements, e.g., sulfur, silicon, oxygen, hydrogen, and carbon, as informed by numerous geophysical and geochemical constraints (recently reviewed by Hirose et al. 2013; Li and Fei 2014; Litasov and Shatskiy 2016). The Fe-C system has been proposed as a candidate composition for the Earth's core largely due to the high cosmochemical abundance of carbon, the frequent occurrence of iron carbide phases in meteorites, and the high solubility of carbon in Fe-Ni liquids under the core-mantle differentiation conditions (Wood 1993). If the liquid core contained carbon, the iron carbide phase, Fe₇C₃, may have been the first phase to crystallize from the iron-carbon melt under core conditions rather than other iron carbide phases such as Fe₃C, as suggested by previously published Fe-C phase diagrams (Fei and Brosh 2014; Lord et al. 2009; Nakajima et al. 2009). The extrapolated density and sound velocity of Fe₇C₃ may account for the density deficit and low S-wave velocity

(v_s) of the inner core (Chen et al. 2012, 2014; Liu et al. 2016a; Nakajima et al. 2011). In addition, its high Poisson's ratio at inner core conditions was suggested to be comparable to that of the inner core (Prescher et al. 2015). Moreover, the melting experiments by Liu et al. (2016b) suggested that Fe₇C₃ may be a constituent of the innermost inner core for a carbon-bearing core composition due to its high melting temperature.

The crystal structure of Fe₇C₃ has remained controversial over the last few decades. Previous experimental studies reported its structure as either hexagonal ($P6_3mc$) (Herbstein and Snyman 1964) or orthorhombic ($Pnma$, $Pmn2_1$, $Pmc2_1$, $Pmcn$, or $Pbca$) (Barinov et al. 2010; Bouchard 1967; Fruchart et al. 1965; Prescher et al. 2015). Theoretical calculations also compared the stability of hexagonal and orthorhombic phases. Fang et al. (2009) determined that the orthorhombic phase ($Pnma$) is more stable than the hexagonal phase ($P6_3mc$), whereas Raza et al. (2015) calculated that the orthorhombic phase (space group $Pbca$) is the stable phase below 100 GPa and the hexagonal phase becomes more stable above 100 GPa.

The elastic constants of Fe₇C₃ were also calculated at 0 K for the two crystal structures with space groups of $P6_3mc$ and $Pbca$ (Mookherjee et al. 2011; Raza et al. 2015). There has been,

however, only one study that calculated the thermoelasticity of Fe$_7$C$_3$ with the space group of *P6$_3$mc* (Li et al. 2016). Most of the high-pressure experimental studies on the density of Fe$_7$C$_3$ were performed at room temperature. The thermal equation of state (EoS) parameters have only been determined below 30 GPa (Litasov et al. 2015; Nakajima et al. 2011), which leads to a large uncertainty when extrapolating the experimental data to the pressure and temperature (*P-T*) conditions of the inner core. Accurate knowledge of the crystal structure and thermoelastic properties of Fe$_7$C$_3$ under core conditions is needed to construct a comprehensive and seismologically consistent Fe-C inner core compositional model.

For the inner core, seismic waves travel faster along the rotational axis than in the equatorial plane; one possible explanation for this anisotropy is the presence of preferentially oriented iron with strong single-crystal elastic anisotropy in the Earth's inner core (Deuss 2014; Hirose et al. 2013). The alloying of light elements with iron often leads to different crystal structure and elasticity (Litasov and Shatskiy 2016). Thus, quantification of the elastic anisotropy of iron alloys is essential for us to understand the inner-core anisotropy. For *hcp* metals and isostructural iron alloys such as the Fe-Ni-Si system, the elastic anisotropy is related to the *c/a* ratio, that is, the compressibilities and thermal expansion of the *a* and *c* unit-cell parameters under high pressure and high temperature (Fischer and Campbell 2015; Steinle-Neumann et al. 2001; Wenk et al. 1988). For orthorhombic Fe$_7$C$_3$, the elastic anisotropy is also correlated with the different compressional response to applied pressure of each primary crystallographic axis as reported in a calculation by Raza et al. (2015). Therefore, it is crucial to constrain how the compressibility and thermal expansion along individual crystallographic axes respond to pressure and temperature, so as to understand the potential for this material to contribute to the seismic anisotropy observed in the inner core (Deuss 2014). In this study, we determined the thermal EoS and the thermoelastic properties of Fe$_7$C$_3$ along different crystallographic axes up to 80 GPa and 800 K by employing an externally heated diamond-anvil cell (DAC) with synchrotron-based single-crystal X-ray diffraction (XRD).

METHODS

The Fe$_7$C$_3$ single-crystal sample was synthesized at 18 GPa and 1773 K in a multi-anvil press (Prescher et al. 2015). Single-crystal XRD characterizations of the sample at ambient conditions were conducted at beamline 13-BMC, the Advanced Photon Source (APS), Argonne National Laboratory, and at the University of Hawai'i at Mānoa (UHM) using a Bruker D8 Venture single-crystal diffractometer (λ = 0.5609 Å). The sample was mounted on a MiTeGen micromesh that was attached to a goniometer head. At beamline 13-BMC, the sample was rotated from –60° to +60°; 120° wide-angle exposure and 1° step exposures were collected. For the ambient characterization of the sample at UHM, a preliminary matrix run was first completed with 1° steps through orthogonal slices of reciprocal space. Indexing of diffraction peaks from the matrix run was used by Bruker APEX 3 software to determine an optimal data collection strategy that ensured 100% completeness to a resolution limit of 0.65 Å. This strategy was then used to collect a full data set.

A BX90 DAC with a pair of 250 μm culet diamond anvils was used for the high-pressure XRD experiments (Kantor et al. 2012). A cubic boron nitride seat on the upstream side and a large-opening tungsten carbide seat on the downstream side were used to maximize access to reciprocal space for the single-crystal XRD measurements. A pyrophyllite ring-heater base was fabricated using a milling machine and sintered in a furnace at 1373 K for 20 h. Three Pt-10 wt% Rh (0.01″) wires were wound around the heater base and covered by high-temperature cement. Two K-type thermocouples (Chromega-Alomega 0.005″ and Chromega-Alomega 0.010″) were mounted near the diamond culet and in touch with the downstream

diamond to measure the temperature. The rhenium gasket was preindented to a thickness of ~35 μm and a sample chamber of 150 μm in diameter was drilled by an electrical discharge machine (EDM). A 10 μm thick Fe$_7$C$_3$ single-crystal grain and two pressure calibrants, a small ruby sphere (Mao et al. 1986) for the neon gas loading and a piece of gold foil near the sample as the primary pressure scale in experiments (Fei et al. 2007), were loaded in the sample chamber. Neon gas, which was used as a pressure-transmitting medium, was loaded in the sample chamber using the gas loading machine at GeoSoilEnviroCARS of the APS. The pressure uncertainties were estimated by the pressure difference between gold and neon (Fei et al. 2007).

The high-pressure and high-temperature synchrotron-based single-crystal XRD experiments were conducted at beamline 13-BMC, APS, Argonne National Lab. The typical size of the focused monochromatic X-ray beam (λ = 0.4340 Å) was 16 × 11 μm^2. A MAR165 charged-coupled device (CCD) detector was used to collect the diffraction patterns. The X-ray accessible opening angle of the DAC was ±20°. The rotation axis for the single-crystal diffraction experiment was placed horizontally, perpendicular to the incident X-ray beam. A series of 10° wide-angle exposures and 1° step exposures from –20° to 20° were collected at four different detector positions for each pressure and temperature point. The investigated range of pressure was 1 bar to 79.2 GPa and range of the temperature was 300 to 800 K (Supplemental[1] Fig. S1).

To analyze the synchrotron-based single-crystal XRD data, we utilized the ATREX software package for peak fitting and intensity corrections (Dera et al. 2013). The unit cell and orientation matrix were determined by the CELL_NOW software (Bruker AXS Inc.). Lattice parameters were refined by least-squares fitting in the RSV software (Dera et al. 2013). The structure refinement was performed using SHELXL (Sheldrick 2008). The ambient-pressure data collected at UHM were analyzed using the Bruker APEX 3 software package to solve the complexity in the crystal structure. The *P-V-T* data and *P-x* (i.e., *a/b/c* axes) were fitted by the EosFit7-GUI program (Gonzalez-Platas et al. 2016).

RESULTS AND DISCUSSION

The crystal structure of Fe$_7$C$_3$ at room pressure and temperature

The indexing of single-crystal XRD patterns of Fe$_7$C$_3$ at ambient conditions indicates an orthorhombic lattice with space group *Pbca* (*Z* = 8) and with unit-cell parameters of *a* = 11.979(1), *b* = 4.5191(8), and *c* = 13.767(2) Å. However, the ambient data indicate some structural complexity beyond the simple ideal structure described previously (Prescher et al. 2015), and consistently present in all of the several single-crystal specimens that we have examined. This non-ideality involves the presence of twin micro-domains but seems to also include structural modulation.

The presence of peaks that could not be indexed using a single orientation matrix to the initially indexed domain indicates a likely twinned crystal structure (Supplemental[1] Fig. S2). The second domain is significantly weaker than the first one. A total of 1651 peaks from the dominant domain were utilized to refine the crystal structure (Fig. 1 and CIF in the deposit materials[1]), which is generally consistent with that reported by Prescher et al. (2015). In the *Pbca* structure, three distorted CFe$_6$ triangular prisms form triads by sharing corners. The triads are stacked parallel to the *b* axis to form a column. Each stack is rotated ~60° relative to its neighbors. Columns are oriented inversely along the *b* axis compared to their neighbor columns. Columns with the same direction are edge sharing and columns with the opposite direction are corner sharing (Fig. 1).

The quality of structural refinement was high (R_{int} = 7.26% and R_1 = 4.97%), however, we noted some artifacts that may be related to the twinning and/or the additional disorder within the structure. Three noticeably large peaks appeared in the difference Fourier map with heights above 2.5 e/Å^3, located about 0.8 Å from carbon atoms, and 1.6 Å from the nearest Fe atoms.
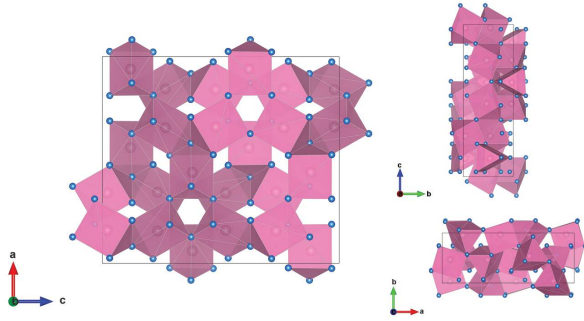
FIGURE 1. The crystal structure of Fe$_7$C$_3$ projected along the *b* axis (left), the *a* axis (upper right), and the *c* axis (lower right) at ambient conditions (space group *Pbca*, *Z* = 8). Blue balls represent Fe. One carbon (pink) is located in the center of each CFe$_6$ triagonal prism colored in pink. (Color online.)

We attempted to reduce the symmetry to allowed orthorhombic and monoclinic subgroups of *Pbca* but could not find an alternative space group that would better account for this difference electron density. We also noted that the residual electron density reported by Prescher et al. (2015) was also quite high (2.022 e/Å^3), which may indicate similar structural complexity in their samples. Proper refinement of such complexity in the structure may require a description using a four-dimensional space group and the introduction of an extra basis vector or modulation vector. Additional ambient pressure experiments at varied temperatures are needed to confirm the likelihood of the modulation and whether the modulation is commensurate or incommensurate. Detailed crystallographic studies will be required to determine the exact origin of this difference electron density, but this is out of the scope for the present study that is primarily focused on the thermoelastic behaviors.

Thermal equation of state of Fe$_7$C$_3$

The unit-cell volumes of Fe$_7$C$_3$ along various isotherms from 300 to 800 K were determined by synchrotron-based single-crystal XRD measurements up to 79.2 GPa (Supplemental[1] Fig. S3 and Table S1). No discontinuous crystal-structure change was observed over the entire pressure and temperature range. The room-temperature *P-V* data were fitted by the third-order Birch-Murnaghan (B-M) EoS:

$$P = \frac{3}{2} K_{T0} \left[\left(\frac{V_{T0}}{V} \right)^{\frac{7}{3}} - \left(\frac{V_{T0}}{V} \right)^{\frac{5}{3}} \right] * \left\{ 1 + \frac{3}{2} (K'_{T0} - 4) \left[\left(\frac{V_{T0}}{V} \right)^{\frac{2}{3}} - 1 \right] \right\} \quad (1)$$

where K_{T0}, K'_{T0}, and V_{T0} are the isothermal bulk modulus, its first pressure derivative and the unit-cell volume at ambient pressure and given temperature *T*, respectively. The 10 *P-V* data were weighted by the uncertainties in both pressure and volume and fitted by the third-order B-M EoS with K_0 = 165(4) GPa, K'_0 = 5.1(2) and V_0 = 745.3(2) Å^3 (K_0, K'_0, and V_0 are for *T* = 300 K). Normalized stress (F_E) as a function of the Eulerian finite strain (f_E) is also plotted as an inset of Figure 2, where f_E = [$(V/V_0)^{-2/3}$ – 1]/2, F_E = P/[$3f_E(1 + 2f_E)^{5/2}$], and the EoS can be simplified as F_E = K_0 + $3K_0/2(K'_0 - 4)f_E$, neglecting the high-order terms (Angel 2000). The *f-F* plot can be used to verify
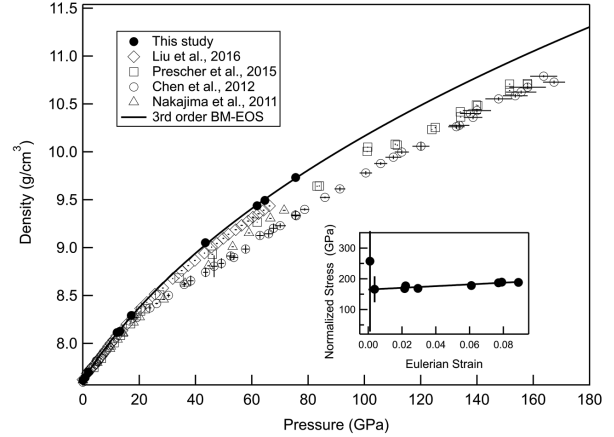

FIGURE 2. Density of the orthorhombic Fe$_7$C$_3$ at 300 K in this study compared with other studies. The fitted density using the third-order Birch-Murnaghan EoS is also displayed as the solid line. The solid circles represent the density of orthorhombic Fe$_7$C$_3$ in this study. The pressure and density uncertainties are mostly within the symbols. The open symbols are from other studies for comparison (Nakajima et al. 2011; Chen et al. 2012; Prescher et al. 2015; Liu et al. 2016a). Inset is the *F-f* plot of data in this study.

which order of the B-M EoS is sufficient to satisfactorily represent the compression behavior of the sample (Angel 2000). The quasi-linear *f-F* relationship suggests the adequacy of using the third-order B-M EoS and its positive slope indicates K'_0 > 4 (Fig. 2 inset). Previous studies reported that the slope of the *f-F* plot changed abruptly as a result of the magnetic transitions of hexagonal Fe$_7$C$_3$ (Chen et al. 2012; Liu et al. 2016a), but we did not observe this, potentially due to the sparsity of our data at 300 K (Fig. 2 inset).

Due to the similarity between the orthorhombic structure with the *Pbca* space group and the hexagonal structure with *P*6$_3$*mc* space group, the compressibility of Fe$_7$C$_3$ was compared with the compressibility of both orthorhombic and hexagonal Fe$_7$C$_3$ in the previous studies (Table 1 and Fig. 2). Our bulk modulus is consistent with the orthorhombic Fe$_7$C$_3$ phase from Prescher et al. (2015), but its pressure derivative, *K'*, is smaller [5.1(2) in this study while 6.1(1) in Prescher et al. (2015)]. The discrepancy may be caused by two reasons. First, we used a gold pressure standard, whereas Prescher et al. (2015) used ruby as their pressure standard. Second, our experiment involved external heating while the experiments in Prescher et al. (2015) were conducted at room temperature. The larger *K'* in their study may indicate less hydrostatic sample chamber with increasing pressure [this is seen in other materials, e.g., Finkelstein et al. 2017]. High temperatures could help to relax the deviatoric stress present in the sample chamber. Comparing with the hexagonal Fe$_7$C$_3$ shown in Figure 2 and Table 1, our density as a function of pressure and compressibility is similar to the values reported by Liu et al. (2016a), who argued that the pressure calibration in his study might be more accurate because the Au pressure standard was placed on the top of the sample.

In our study, Equation 1 was used along with various high-temperature isotherms at 300, 400, 500, 600, 700, and 800 K (Supplemental Table S1 and Fig. 3). Assuming that d*K*/d*T* is

TABLE 1. The thermoelastic properties of Fe_7C_3 compared with previous studies

	P range (GPa)	T range (K)	K_0 (GPa)	K_0'	Normalized V_0 (Å³)[a]	Thermoelastic properties	Method	Reference
					Orthorhomic (*Pbca*)			
	0–79.2	300	165(4)	5.1(2)	93.2(3)	–	SCXRD+DAC	This study
	0–79.2	300–800	167(4)	5.0(2)	93.2(3)	$dK/dT = -0.02(1)$ GPa/K $a_0 = 4.7(9)\cdot10^{-5}$ K^{-1} $a_1 = 3(5)\cdot10^{-8}$ K^{-2} [b]	SCXRD+DAC	This study
	4–158	300	168(4)	6.1(1)	93.1 (1)	–	SCXRD+DAC	Prescher et al. (2015)
					Hexagonal (*P6₃mc*)			
ferromagnetic	0–18	300	201(2)	4 (fixed)	93.2(1)		PXRD+DAC+multi-anvil press	Nakajima et al. (2011)
paramagnetic	18–71.5	300–1973	253(7)	3.6(2)	92.1(3)	$\gamma_0 = 2.57(5)$ $\theta = 920 (140)$ K $q = 2.2(5)$	PXRD+DAC+multi-anvil press	Nakajima et al. (2011)
ferromagnetic			231	4.4	91			
nonmagnetic			291	4.5	88			
paramagnetic	7–53	300	201(12)	8.0(1.4)	92.4(2)	–	SCXRD+DAC	Chen et al. (2012)
nonmagnetic	53–167	300	307(6)	3.2(1)	91.5(4)	–	SCXRD+DAC	Chen et al. (2012)
	0	297–911	–	–		$a_0 = 3.1(6)\cdot10^{-5}$ K^{-1} $a_1 = 1.2(6)\cdot10^{-8}$ K^{-2} [c]	PXRD	Litasov et al. (2015)
ferromagnetic	0–7	300	186(5)	6.9(2.2)	93.1(1)	–	PXRD+DAC	Liu et al. (2016a)
noncollinear	7–20	300	166(13)	4.9(1.1)	93.5(4)	–	PXRD +DAC	Liu et al. (2016a)
paramagnetic	20–66	300	196(9)	4.9(2)	92.3(5)	–	PXRD +DAC	Liu et al. (2016a)

Notes: SCXRD and PXRD are acronyms of single-crystal XRD and powder XRD, respectively.
[a] Normalized V_0 represents volume per Fe_7C_3 formula.
[b] The coefficient of thermal expansion was calculated as $\alpha = \alpha_0 + \alpha_1 \times (T-300)$.
[c] The coefficient of thermal expansion was calculated as $\alpha = \alpha_0 + \alpha_1 \times T$.

constant through the temperature ranges, K_{T0} and K'_{T0} can be described as:

$$K_{T0} = K_0 + dK/dT \times (T-300) \tag{2}$$
$$K'_{T0} = K'_0 \tag{3}$$

and the temperature dependence of volume can be expressed by the empirical polynomial equation (Berman 1988) as:

$$V_{T0} = V_0[1 + a_0(T-300) + \tfrac{1}{2}a_1(T-300)^2]. \tag{4}$$

Taking the first derivative of Equation 4 gives the thermal expansion coefficient $\alpha_T = \alpha_0 + \alpha_1(T-300)$ by approximation. The fit to the *P-V-T* data (Supplemental[1] Table S1) using Equations 1–4 results in $K_0 = 167(4)$ GPa, $K'_0 = 5.0(2)$, $V_0 = 745.2(2)$ Å³, $dK/dT = -0.02(1)$ GPa/K, and thermal expansion $\alpha_T = 4.7(9) \times 10^{-5} + 3(5) \times 10^{-8} \times (T-300)$ K^{-1}. K_0, K'_0, and V_0 obtained by the high-temperature Birch-Murnaghan EoS are consistent with the values by only fitting the 300 K data within the uncertainties.

Compressibilities and thermal expansions of the *a, b,* and *c* axes

The compression data of the *a*, *b*, and *c* axes at 300 K were fitted by the EosFit7-GUI program (Gonzalez-Platas et al. 2016). The program fits the cube of the lattice parameters to obtain the linear moduli and its pressure derivative, typically denoted as M and M', respectively (Angel et al. 2014). M is the inverse of the linear compressibility β [$\beta_i = x_i^{-1}(\partial x_i/\partial P)_T$] and three times that of the volume-like K value (Angel 2000). The fitting yields $M_a = 577(14)$ GPa, $M'_a = 18.6(9)$, $M_b = 438(9)$ GPa, $M'_b = 12.7(4)$, $M_c = 490(32)$ GPa and $M'_c = 16(2)$. $M_a > M_c > M_b$ indicates that the axial compressibilities of Fe_7C_3 are anisotropic (Fig. 4). Considering the trade-off between M and M', compressibilities of the *a*, *b*, and *c* axes are distinguishable from each other (Fig. 4a inset). Given that $M'_a > M'_c > M'_b$ and
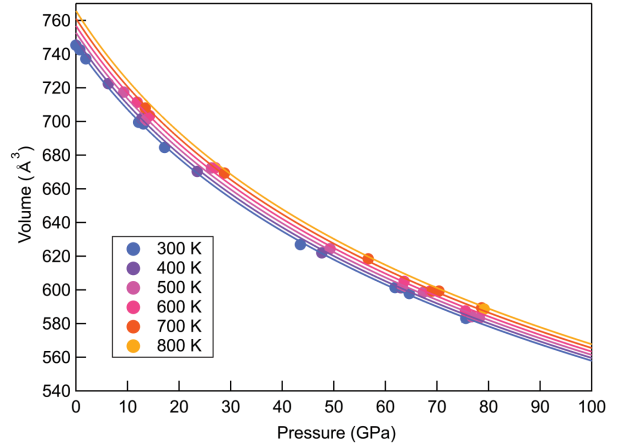

FIGURE 3. The *P-V-T* data of Fe_7C_3 fitted by the high-temperature Birch-Murnaghan EoS. The pressure and volume uncertainties are within the symbols. Solid curves are the fitting results. (Color online.)

considering their magnitudes, the *b* axis would stay the most compressible, ~17.4% smaller than the *c* axis, and ~26.5% smaller than the *a* axis in linear modulus at 330–364 GPa (Fig. 4b). The reason that the *a* and *c* axes are less compressible than the *b* axis is that Fe ions are distributed more densely in the same *a-c* plane than in the *b* direction, which makes the Fe-Fe bonds shorter and stronger in *a* and *c* directions (Fig. 1). Similar to our results, theoretical calculations by Raza et al. (2015) also indicated that the axial compressibilities of the orthorhombic Fe_7C_3 are discernably anisotropic, and the compressibility of the *b* axis is most obviously different from those of the other axes. The calculated sound velocity (v_p) of Fe_7C_3 in *b* direction is the slowest, while the sound velocities in the *a* and *c* directions are relatively similar at 360 GPa (Raza et al. 2015), which is consistent with our linear incompressibility results.
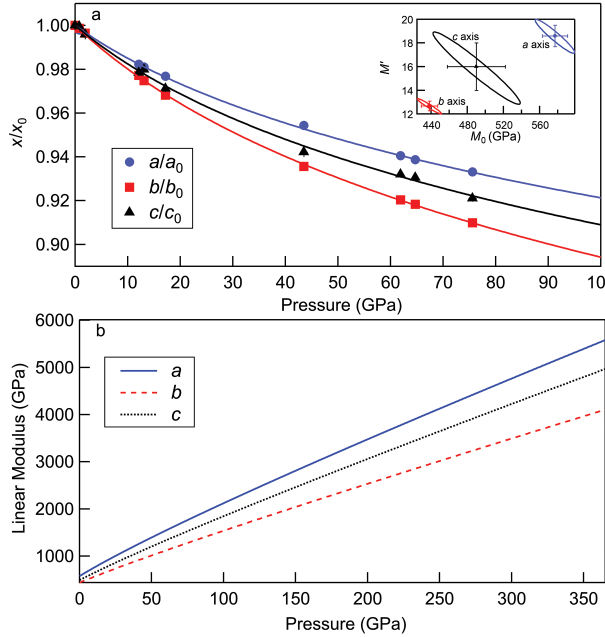
FIGURE 4. The compressibilities of the a, b, and c axes of Fe_7C_3 as a function of pressure. (**a**) The variation of a/a_0, b/b_0, and c/c_0 as a function of pressure were fitted by the linear EoS. The uncertainties are mostly within the symbols. Inset: the confidence ellipses for the a, b, and c axes, illustrating the trade-off between M_0 and M'. (**b**) The calculated and extrapolated linear moduli of the a, b, and c axes as a function of pressure. (Color online.)

Thermal expansion coefficients of a^3, b^3, and c^3 are also calculated using Equation 5 (Fig. 5):

$$\alpha = \frac{x_{T(P)}^3 - x_{0(P)}^3}{x_{0(P)}^3 (T - T_0)}. \tag{5}$$

We found that the thermal expansions of c^3 (about 8×10^{-5} K^{-1}) from 300 to 600 or 700 K were larger than that of a^3 and b^3 by a factor of approximately 4, indicating that there are anisotropic responses of lattice expansion to high temperature along different crystallographic directions (Fig. 6). The anisotropic response was also reflected by an increase in the c/a ratio upon heating (Fig. 7). The b/a ratio was nearly unchanged with temperature and the b/c ratio decreased with temperature (Fig. 7). This means that the significant change of the c/a ratio with temperature can be mainly attributed to the large expansion of the c axis upon heating.

The distinct anisotropic responses could influence the compressibility and sound velocities of Fe_7C_3. For hcp iron, the c/a ratio also increases upon heating and the elastic anisotropy changes, showing that the corresponding longitudinal modulus of c axis, C_{33} decreases and becomes smaller than C_{11} (Steinle-Neumann et al. 2001). This suggests that an expanded c axis may result in elastic softening along this crystallographic direction. One consequence might be a larger sound velocity reduction along the c axis than the other axes at high temperatures. Although the crystal structure of hcp iron is different from that of Fe_7C_3, the change of the c/a ratios upon heating in Fe_7C_3, resulted from the compressibilities change of the crystallographic axis, may still indicate the change of the elastic anisotropy.
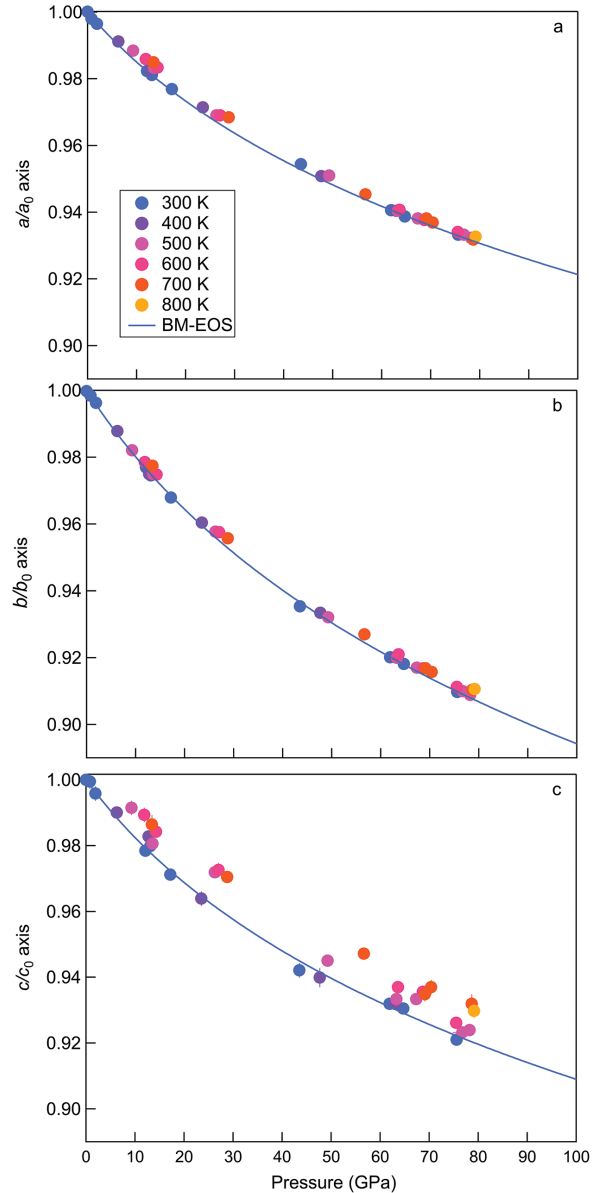

FIGURE 5. The high-temperature (**a**) a/a_0, (**b**) b/b_0, and (**c**) c/c_0 of Fe_7C_3 vs. pressure. The room-temperature data were fitted by the linear EoS. (Color online.)

Along the isotherms, the c/a ratio gradually decreases up to ~40 GPa and then increases abruptly (Fig. 7), probably due to the high-spin to low-spin transition of Fe_7C_3 (Chen et al. 2012, 2014). For higher temperature data, the change occurs at higher pressures: this is consistent with that high temperature would promote the high-spin to low-spin transition in 3d metal compounds (Gütlich et al. 1994) and probably indicates a positive slope for the spin transition (Liu et al. 2016a). The spin transition may have lead to the kink in the c/a ratio at ~40 GPa at 300 K (Fig. 7). After the spin transition, it appears that the c/a ratio decreases at a similar slope as that before the spin transition. The effect of the spin transition on the compressibilities of crystallographic axes is
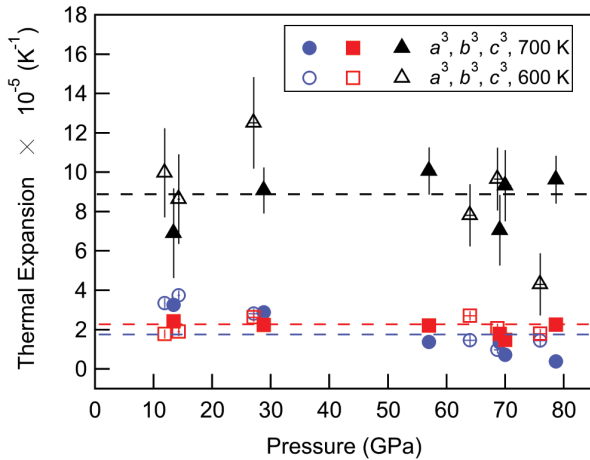
FIGURE 6. Thermal expansion of a^3, b^3, and c^3 axes of Fe₇C₃ at 600 and 700 K. Open symbols represent the calculated thermal expansion for different axes. Dashed lines are guide lines showing the thermal expansion of c^3 is approximately 4 times larger than a^3 and b^3. (Color online.)

not obvious in this study. We found it was reasonable to use one linear equation of state to describe the compressibility of each crystallographic axis (Fig. 4). Further studies with denser data coverage and to higher pressure are required to further confirm that intepretation.

Temperature may significantly influence the elastic properties of Fe₇C₃ at high pressures. When only pressure is taken into account, the a and c axes of Fe₇C₃ have relatively similar compressibilities, but the b axis is more compressible. According to theoretical calculations, the b axis is also the direction that acoustic waves travel the slowest (Raza et al. 2015). When temperature is considered, the c axis expands more significantly than the other axes and thus becomes elastically softer at high temperatures, which suggests that the acoustic wave traveling along the c axis may also slow down and influence the elastic anisotropy. At high-pressure and high-temperature conditions like in the inner core, the a axis of Fe₇C₃ will stay the most incompressible and thus have the highest axial sound velocity. Our data implies that temperature is an important factor when considering the anisotropy of Fe₇C₃ at core conditions and caution needs to be exercised when extrapolating to the inner-core conditions.

GEOPHYSICAL IMPLICATIONS FOR THE EARTH'S INNER CORE

Seismological data suggest that the Earth's inner core exhibits strong elastic anisotropy, an anomalously high Poisson's ratio, and low shear-wave velocity (v_S) [Deuss (2014) and the papers cited within]. These seismic features are possibly linked to the crystallographic anisotropy of the inner-core crystals. According to the theoretically calculated Fe-C phase diagram at 330 GPa, if a Fe-C liquid has >2 wt% carbon, Fe₇C₃ would crystallize first to form an iron carbide inner core (Fei and Brosh 2014); the innermost inner core has been further suggested to be Fe₇C₃ based on the melting experiments of the Fe-C system to core pressures (Liu et al. 2016b). With decreasing core temperature and the depletion of carbon in the outer core by the growth of Fe₇C₃ in the inner core, the Fe-C melt will approach the eutectic
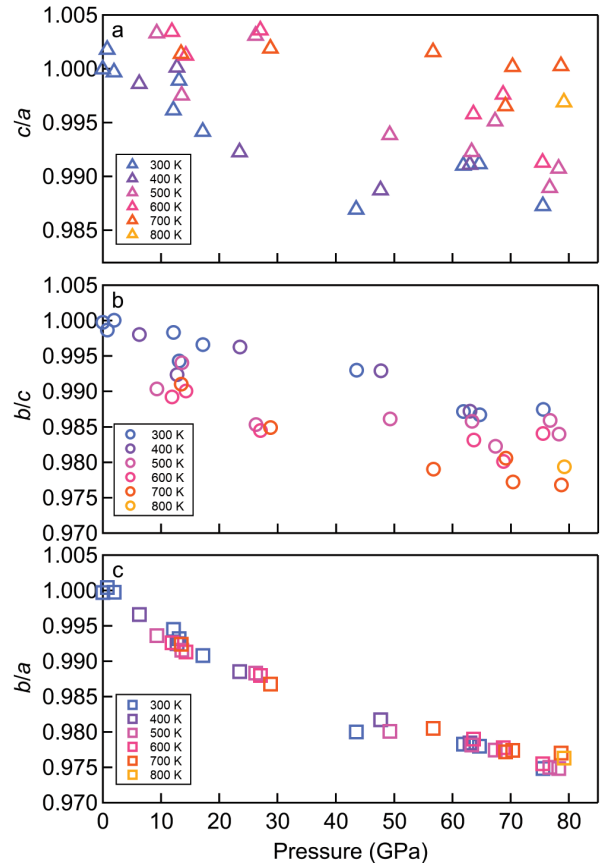

FIGURE 7. The (**a**) c/a ratio, (**b**) b/c ratio, and (**c**) b/a ratio of Fe₇C₃ up to 800 K as a function of pressure. (Color online.)

composition. C-doped Fe and Fe₇C₃ would crystallize from the eutectic composition and form the outer part of the inner core that surrounds the innermost inner core. Our results on the anisotropic compressibility and thermal expansion of the different crystallographic axes of Fe₇C₃ may provide an explanation for the seismic observations of the inner core, particularly the observed inner core anisotropy. The effect of temperature on the elastic properties and anisotropy of Fe alloys such as Fe₇C₃ are crucial for us to construct a seismologically consistent core compositional model and thus inform a better understanding of the composition and structure of the inner core. The thermal expansions of iron carbides at high pressures are crucial for modeling the Fe-C phase relations at extreme conditions (Fei and Brosh 2014), which may inform our understanding of the mineralogy of the inner core and the role of carbon during inner core crystallization.

REFERENCES CITED

Angel, R.J. (2000) Equations of state. Reviews in Mineralogy and Geochemistry, 41(1), 35–59.

Angel, R.J., Alvaro, M., and Gonzalez-Platas, J. (2014) EosFit7c and a Fortran module (library) for equation of state calculations. Zeitschrift für Kristallographie-Crystalline Materials, 229(5), 405–419.

Barinov, V., Tsurin, V., and Surikov, V. (2010) Study of mechanically synthesized carbide Fe$_7$C$_3$. The Physics of Metals and Metallography, 110(5), 474–484.

Berman, R.G. (1988) Internally-consistent thermodynamic data for minerals in the system Na$_2$O-K$_2$O-CaO-MgO-FeO-Fe$_2$O$_3$-Al$_2$O$_3$-SiO$_2$-TiO$_2$-H$_2$O-CO$_2$. Journal of Petrology, 29(2), 445–522.

Bouchard, J. (1967) Etude structurale des carbures de manganese. Annales de Chimie, 2, 353–366.

Chen, B., Gao, L., Lavina, B., Dera, P., Alp, E.E., Zhao, J., and Li, J. (2012) Magneto-elastic coupling in compressed Fe$_7$C$_3$ supports carbon in Earth's inner core. Geophysical Research Letters, 39(18).

Chen, B., Li, Z., Zhang, D., Liu, J., Hu, M.Y., Zhao, J., Bi, W., Alp, E.E., Xiao, Y., and Chow, P. (2014) Hidden carbon in Earth's inner core revealed by shear softening in dense Fe$_7$C$_3$. Proceedings of the National Academy of Sciences, 111(50), 17755–17758.

Dera, P., Zhuravlev, K., Prakapenka, V., Rivers, M.L., Finkelstein, G.J., Grubor-Urosevic, O., Tschauner, O., Clark, S.M., and Downs, R.T. (2013) High pressure single-crystal micro X-ray diffraction analysis with GSE_ADA/RSV software. High Pressure Research, 33(3), 466–484.

Deuss, A. (2014) Heterogeneity and anisotropy of Earth's inner core. Annual Review of Earth and Planetary Sciences, 42, 103–126.

Fang, C.M., Van Huis, M.A., and Zandbergen, H.W. (2009) Structural, electronic, and magnetic properties of iron carbide Fe$_7$C$_3$ phases from first-principles theory. Physical Review B, 80(22), 224108.

Fei, Y., and Brosh, E. (2014) Experimental study and thermodynamic calculations of phase relations in the Fe–C system at high pressure. Earth and Planetary Science Letters, 408, 155–162.

Fei, Y., Ricolleau, A., Frank, M., Mibe, K., Shen, G., and Prakapenka, V. (2007) Toward an internally consistent pressure scale. Proceedings of the National Academy of Sciences, 104(22), 9182–9186.

Finkelstein, G.J., Jackson, J.M., Sturhahn, W., Zhang, D., Alp, E.E., and Toellner, T.S. (2017) Single-crystal equations of state of magnesiowüstite at high pressures. American Mineralogist, 102(8), 1709–1717.

Fischer, R.A., and Campbell, A.J. (2015) The axial ratio of hcp Fe and Fe–Ni–Si alloys to the conditions of Earth's inner core. American Mineralogist, 100, 2718–2724.

Fruchart, R., Senateur, J., Bouchaud, J., and Michel, A. (1965) A propos de la structure exacte du carbure de fer Fe$_7$C$_3$. Bulletin de la Societe Chimique de France (2), 392.

Gonzalez-Platas, J., Alvaro, M., Nestola, F., and Angel, R. (2016) EosFit7-GUI: a new graphical user interface for equation of state calculations, analyses and teaching. Journal of Applied Crystallography, 49(4), 1377–1382.

Gütlich, P., Hauser, A., and Spiering, H. (1994) Thermal and optical switching of iron (II) complexes. Angewandte Chemie International Edition in English, 33(20), 2024–2054.

Herbstein, F., and Snyman, J. (1964) Identification of Eckstrom-Adcock iron carbide as Fe$_7$C$_3$. Inorganic Chemistry, 3(6), 894–896.

Hirose, K., Labrosse, S., and Hernlund, J. (2013) Composition and state of the core. Annual Review of Earth and Planetary Sciences, 41, 657–691.

Kantor, I., Prakapenka, V., Kantor, A., Dera, P., Kurnosov, A., Sinogeikin, S., Dubrovinskaia, N., and Dubrovinsky, L. (2012) BX90: A new diamond anvil cell design for X-ray diffraction and optical measurements. Review of Scientific Instruments, 83(12), 125102.

Li, J., and Fei, Y. (2014) Experimental Constraints on Core Composition, p. 527–557. Elsevier.

Li, Y., Vočadlo, L., Brodholt, J., and Wood, I. (2016) Thermoelasticity of Fe$_7$C$_3$ under inner core conditions. Journal of Geophysical Research: Solid Earth, 121(8), 5828–5837.

Litasov, K.D., and Shatskiy, A. (2016) Composition of the Earth's core: A review. Russian Geology and Geophysics, 57(1), 22–46.

Litasov, K.D., Rashchenko, S.V., Shmakov, A.N., Palyanov, Y.N., and Sokol, A.G. (2015) Thermal expansion of iron carbides, Fe$_7$C$_3$ and Fe$_3$C, at 297–911K determined by in situ X-ray diffraction. Journal of Alloys and Compounds, 628, 102–106.

Liu, J., Li, J., and Ikuta, D. (2016a) Elastic softening in Fe$_7$C$_3$ with implications for Earth's deep carbon reservoirs. Journal of Geophysical Research: Solid Earth, 121(3), 1514–1524.

Liu, J., Lin, J.F., Prakapenka, V., Prescher, C., and Yoshino, T. (2016b) Phase relations of Fe$_3$C and Fe$_7$C$_3$ up to 185 GPa and 5200 K: Implication for the stability of iron carbide in the Earth's core. Geophysical Research Letters, 43(24), 12,415–12,422.

Lord, O., Walter, M., Dasgupta, R., Walker, D., and Clark, S. (2009) Melting in the Fe–C system to 70 GPa. Earth and Planetary Science Letters, 284(1), 157–167.

Mao, H., Xu, J.-A., and Bell, P. (1986) Calibration of the ruby pressure gauge to 800 kbar under quasi-hydrostatic conditions. Journal of Geophysical Research: Solid Earth, 91(B5), 4673–4676.

Mookherjee, M., Nakajima, Y., Steinle-Neumann, G., Glazyrin, K., Wu, X., Dubrovinsky, L., McCammon, C., and Chumakov, A. (2011) High-pressure behavior of iron carbide (Fe$_7$C$_3$) at inner core conditions. Journal of Geophysical Research: Solid Earth, 116, B04201.

Nakajima, Y., Takahashi, E., Sata, N., Nishihara, Y., Hirose, K., Funakoshi, K., and Ohishi, Y. (2011) Thermoelastic property and high-pressure stability of Fe$_7$C$_3$: Implication for iron-carbide in the Earth's core. American Mineralogist, 96(7), 1158–1165.

Nakajima, Y., Takahashi, E., Suzuki, T., and Funakoshi, K.-i. (2009) "Carbon in the core" revisited. Physics of the Earth and Planetary Interiors, 174(1), 202–211.

Prescher, C., Dubrovinsky, L., Bykova, E., Kupenko, I., Glazyrin, K., Kantor, A., McCammon, C., Mookherjee, M., Nakajima, Y., and Miyajima, N. (2015) High Poisson's ratio of Earth's inner core explained by carbon alloying. Nature Geoscience, 8(3), 220–223.

Raza, Z., Shulumba, N., Caffrey, N.M., Dubrovinsky, L., and Abrikosov, I.A. (2015) First-principles calculations of properties of orthorhombic iron carbide Fe$_7$C$_3$ at the Earth's core conditions. Physical Review B, 91(21), 214112.

Sheldrick, G.M. (2008) A short history of SHELX. Acta Crystallographica, A64, 112–122.

Steinle-Neumann, G., Stixrude, L., Cohen, R., and Gülseren, O. (2001) Elasticity of iron at the temperature of the Earth's inner core. Nature, 413, 57.

Wenk, H., Takeshita, T., Jeanloz, R., and Johnson, G. (1988) Development of texture and elastic anisotropy during deformation of hcp metals. Geophysical Research Letters, 15(1), 76–79.

Wood, B.J. (1993) Carbon in the core. Earth and Planetary Science Letters, 117(3), 593–607.

Endnote:

[1]Deposit item AM-18-106527, Supplemental Material and CIF. Deposit items are free to all readers and found on the MSA web site, via the specific issue's Table of Contents (go to http://www.minsocam.org/MSA/AmMin/TOC/2018/Oct2018_data/ Oct2018_data.html).